Nonlinear Filtering of Light-Curve Data

Sehyun Yun[1,*], Renato Zanetti[2]

Aerospace Engineering and Engineering Mechanics Department, Cockrell School of Engineering,
The University of Texas at Austin, Austin, Texas 78712

Abstract

A particle filter with an expectation-maximization (EM) clustering algorithm to approximate the state's distribution with Gaussian mixture models (GMMs) is proposed to simultaneously estimate the position, velocity, attitude, angular rates, and surface parameters of a space object (SO) in the near-Geostationary Earth Orbit (GEO). Recent work shows that the unscented Kalman filter applied to this problem is susceptible to divergence due to the presence of the many uncertain states estimated. The underlying reasons of the filter's divergence have not yet been completely revealed and preliminary attributed to information dilution. Under the scenario considered in this paper, it is demonstrated through numerical simulation that the underlying reason for the filter's divergence in SO tracking is due to the severe nonlinearities of light-curve measurement data coupled with weak observability; rather than information dilution. In addition to the novel particle filter, two alternative estimation techniques based on modifications of the extended Kalman filter (EKF) and unscented Kalman filter (UKF) are introduced to reduce the computational burden while still mitigating filter divergence.

Keywords: Space situational awareness, Information dilution theorem, Particle filter, Gaussian mixture models

1. Introduction

Space situational awareness (SSA) refers to knowledge of our near-space environment, including the tracking and identification of space objects (SOs) orbiting Earth. This task encounters many challenges and one of them is the limited number of sensors available to track and identify an ever growing number of SOs. To extract as much information as possible from the sparse data, sophisticated techniques need to be used to estimate and predict the states of SOs. Precise models of non-gravitational forces acting on SOs are needed for accurate orbit prediction and propagation. Solar radiation pressure (SRP) is the main non-gravitational force acting on SOs in or around Geostationary Earth Orbits (GEO) and it can be modeled using the shape and reflectivity properties of the body (McMahon and Scheeres, 2015; Kelecy et al., 2012).

Light curve data, which is an object's observed brightness, have been used to analyze attitude observability and

---

[*] Corresponding author
Email addresses: `shyun@utexas.edu` (Sehyun Yun), `renato@utexas.edu` (Renato Zanetti)

[1] Ph.D. student, Department of Aerospace Engineering and Engineering Mechanics

[2] Assistant Professor, Department of Aerospace Engineering and Engineering Mechanics

to estimate the shape and attitude of SOs (Hinks et al., 2013; Wetterer and Jah, 2009; Linares et al., 2014d; Fan and Frueh, 2019; Linares et al., 2013). Since light curve observations are sensitive to the object's surface parameters, these can also be estimated from light curve data (Wetterer et al., 2014; Linares and Crassidis, 2018). Furthermore, it is shown that the space object mass as well as the position, velocity, angle, angular velocity and surface parameters can be estimated by fusing the two data types, the angles (line-of-sight) and apparent brightness magnitude of an object (Linares et al., 2012, 2014b,c). Estimation of this many parameters with relatively little observations variety, however, has been shown to cause diverged in an unscented Kalman filter (UKF) when too many states with large uncertainty are estimated simultaneusly (Wetterer et al., 2013). Wetterer et al. (2013) attributes the divergence to information dilution (Fraiture, 1986).

According to the information dilution theorem (IDT), when additional biases are added to an estimation problem, it is possible that the uncertainties of the original states in the model increase (Rapoport and Bar-Itzhack, 2001). Moreover, filter divergence may occur because the limited information is not being used in the most proper way (Wetterer et al., 2013). To resolve the information dilution problem in the context of SO tracking, multiple-model adaptive estimation (MMAE) and unscented Schmidt-Kalman filter were implemented to determine which states should be estimated (Linares et al., 2014d; Dianetti et al., 2018; Mallik and Jah, 2019; Richardson et al., 2019). Dianetti et al. (2018) quantifies system observability with the information matrix of an estimator and uses the system's observability to determine which states should be estimated. Mallik and Jah (2019) use an unscented Schmidt-Kalman filter algorithm based on the physical relationship between SRP and observed albedo-area to find low observable states and to consider their contribution to the uncertainty of the system without estimating them. The Schmidt-Kalman filter (Schmidt, 1966) only estimates a subset of the states, while "considers" the effect of other statess without attempting to infer their value; with this approach the effective number of estimated states is reduced and the effects of information dilution are mitigated. Richardson et al. (2019) also employ an unscented Schmidt-Kalman filter algorithm and use the Fisher information matrix (FIM) to measure of the observability of the system; when the FIM becomes close to singular, some states are considered rather than estimated. Considering states in a recursive estimator mitigates information dilution, and to date no study exists that conclusively establishes whether concurrently estimating a dynamic attitude state, angular velocity, and surface parameters from light curve data using a recursive estimator is feasible or if, conversely, information dilution and/or the lack of observability prevent such an estimator to improve knowledge of the system or even avoid divergence. In this paper, we demonstrate that the principal driver to divergence is the severe nonlinearity of the problem and that it is possible to design a recursive estimator able to improve knowledge of both the attitude and the surface parameters of SOs. The detrimental effects of nonlinearities are exacerbated by information dilution making the UKF design in Wetterer et al. (2013) diverge, but information dilution alone is not cause for divergence; as shown by the algorithms proposed in this work. In this work, the system is studied using three different recursive estimation techniques that successfully estimate all states simultaneously without resorting to only consider the uncertainty of some of them. The three algorithms used are: a newly proposed modification of particle filter with Gaussian mixture models (PFGMM) (Raihan and Chakravorty, 2018), the truncated interval unscented Kalman filter (TIUKF) (Teixeira et al., 2010), and the truncated extended Kalman filter (TEKF) (Simon and Simon, 2010).

The first estimation technique used here is based on sequential Monte Carlo methods. Previous works using sequential Monte Carlo methods include Linares et al. (2014a), where attitude and angular velocity of an SO are estimated from light curve data using a regularized particle filter with the generalized Rodrigues parameters used for local attitude error representation. More recently, a marginalized particle filter is used to reduce computational cost of a conventional particle filter (PF) for attitude and angular velocity estimation from light curve data (Coder et al., 2018a,b). The use of a PF in this type of problems is particularly appealing for two reasons: i. it provides a nonlinear approximation of the optimal nonlinear estimator, and ii. it handles much larger initial uncertainties than linear estimators (such as the extended Kalman filter (EKF) or the UKF); in fact, Coder et al. (2018a) assume a a uniform initial attitude uncertainty of almost 360 degrees. Coder et al. (2018a,b) are very successful in estimating attitude, but do not attempt to concurrently estimate both attitude and surface parameters. It is the addition of surface parameters that causes information dilution and divergence in Wetterer et al. (2013). This work also uses a sequential Monte Carlo filter to estimate both the attitude and rate of the vehicle, but the filter's estimated states include surface parameters and translational states. Surface parameters are successfully estimated in (Wetterer et al., 2014) and (Linares and Crassidis, 2018); the former uses multiple model adaptive estimation, essentially choosing between a finite set of possible values for the surface parameters, while the latter is perhaps the closest existing results to this work. The key differences between the two works is that Linares and Crassidis (2018) assume a known (constant) angular velocity, hence the attitude estimation problem can be fully solved by determining the attitude at a single time; therefore all estimated quantities are constant/static, and a batch approach for Bayesian inverse problems is used by the authors. This work, on the other hand, does not assume a priori knowledge of the angular velocity, which is instead estimated together with the attitude and surface parameters in a recursive dynamic filter.

The proposed sequential Monte Carlo method is a modification of the work by Raihan and Chakravorty (2018) but a different clustering algorithm (expectation-maximization, EM) is used to form the Gaussian Mixture Model (GMM) density approximation. This modification overcomes issues encountered when applying to this problem two existing particle/GMM hybrid algorithms, Yun and Zanetti (2019) and Raihan and Chakravorty (2018). Yun and Zanetti (2019) introduces a new sequential Monte Carlo algorithm which treats each particle of the pre-propagation distribution as a Gaussian component with a zero or small covariance matrix; the Gaussian sum filter (GSF) algorithm is used to calculate the posterior distribution. Raihan and Chakravorty (2018) introduces the particle Gaussian mixture filter (PGMF) and employs an ensemble of randomly sampled states for the propagation of the conditional state probability density. The propagated ensemble for representing the propagated PDF is clustered using K-means algorithm. While K-means is a simple approach to clustering, it does not produce adequate results for the problem at hand. The K-means algorithm performs a hard assignment of data points to clusters, which means each data point is associated uniquely with one cluster, hence only the points in the same cluster are used to update each mean. Additionally, the K-means algorithm does not account for the covariance. The K-means algorithm can be interpreted as a special case of GMMs clustering in which all mixture weights are equal and the covariance matrices of the mixture components are given by ξI, where ξ is a variance parameter and I is the identity matrix. The EM algorithm for GMMs used in this paper as it performs a soft assignment based on the posterior probabilities, thus obtaining the proper covariance of the components. In addition, to this new nonlinear filter, the modified UKF and EKF are also shown to successfully mitigate the filter divergence issues while reducing the overall computational complexity.

The remainder of this paper is organized as follows. First, the dynamics and measurement models are described and the filter states are presented. Then, the various nonlinear estimation techniques are introduced in section III. In section IV, simulation results are shown using five filtering algorithms followed by some concluding remarks on the methodology and results.

2. System Models

In this paper, the inertial position and velocity of SOs are denoted by $\boldsymbol{r}^I = [x\ y\ z]^{\mathrm{T}}$ and $\boldsymbol{v}^I = [v_x\ v_y\ v_z]^{\mathrm{T}}$, respectively. The quaternion, which is based on the Euler axis of rotation $\boldsymbol{n}$ and rotation angle θ, is defined as $\boldsymbol{q} = \left[\sin(\theta/2)\boldsymbol{n}^{\mathrm{T}}\ \cos(\theta/2)\right]^{\mathrm{T}} = \left[\boldsymbol{\varrho}^{\mathrm{T}}\ q\right]^{\mathrm{T}}$ and the angular velocity of the SO with respect to the inertial frame, expressed in body frame, is denoted by $\boldsymbol{\omega}^B_{B/I} = [\omega_x\ \omega_y\ \omega_z]^{\mathrm{T}}$.

2.1. Dynamics Model

The orbital dynamics of SO in Earth-centered inertial (ECI) coordinates are modeled by

$$\ddot{\boldsymbol{r}}^I = -\frac{\mu}{r^3}\boldsymbol{r}^I + \boldsymbol{a}^I_{J_2} + \boldsymbol{a}^I_{srp} \tag{1}$$

where μ is the Earth's gravitational parameter, r is the Euclidean norm of $\boldsymbol{r}^I$, $\boldsymbol{a}^I_{J_2}$ is the gravitational perturbation due to non-spherical nature of Earth, and $\boldsymbol{a}^I_{srp}$ is the acceleration perturbation due to SRP.

The J_2 perturbation acceleration equation computes the three component forces in the ECI frame.

$$\ddot{x} = F\left(1 - 5\left(\frac{z}{r}\right)^2\right)\frac{x}{r} \tag{2}$$

$$\ddot{y} = F\left(1 - 5\left(\frac{z}{r}\right)^2\right)\frac{y}{r} \tag{3}$$

$$\ddot{z} = F\left(3 - 5\left(\frac{z}{r}\right)^2\right)\frac{z}{r} \tag{4}$$

where

$$F = -\frac{3}{2}J_2\left(\frac{\mu}{r^2}\right)^2\left(\frac{R_E}{r}\right)^2 \tag{5}$$

where J_2 is the second zonal harmonic coefficient and R_E is the Earth's equatorial radius. Higher order spherical harmonics are neglected without loss of generality. At geosynchrounous distances, the J_2 term is almost negligible and higher order spherical harmonics are not needed to demonstrate the efficacy of the proposed methodologies.

SRP represents the primary non-gravitational force acting on SOs in GEO and the acceleration due to SRP is modeled using the shape of the body. In this paper, it is assumed that the shape model consists of a finite number of flat facets; the i^{th} facet is defined by a set of three orthonormal basis vectors $\boldsymbol{u}^B_u$, $\boldsymbol{u}^B_v$, and $\boldsymbol{u}^B_n$ expressed in the body coordinates. The unit vector $\boldsymbol{u}^B_n$ points outward normal of the facet, whereas the vectors $\boldsymbol{u}^B_u$ and $\boldsymbol{u}^B_v$ lie in the plane

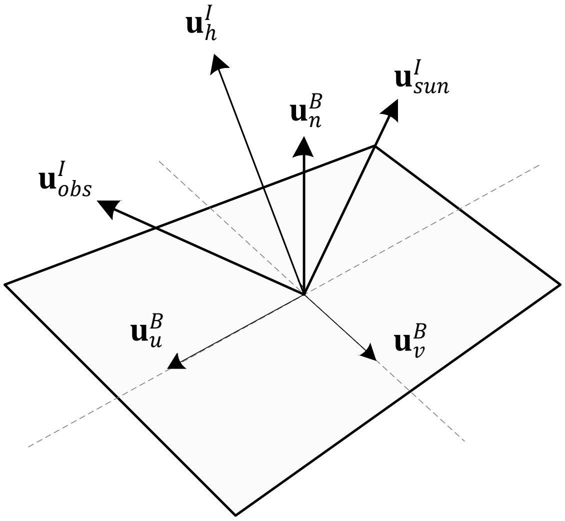

Figure 1: Geometry of reflection

of the facet. The geometry of the modeled reflection is shown in Figure 1. The acceleration perturbation due to SRP is then given by (Wetterer et al., 2013):

$$\boldsymbol{a}_{srp}^I = \sum_{i=1}^{N_{facets}} \boldsymbol{a}_{srp}^I(i) \tag{6}$$

$$\boldsymbol{a}_{srp}^I(i) = -\frac{S_F \mathcal{A}(i)\left(\boldsymbol{u}_n^I(i)\cdot\boldsymbol{u}_{sun}^I\right)}{mc}\left(\left(1 - sF_0\right)\boldsymbol{u}_{sun}^I + \left(\frac{2}{3}d\rho + 2sF_0\left(\boldsymbol{u}_n^I(i)\cdot\boldsymbol{u}_{sun}^I\right)\right)\boldsymbol{u}_n^I(i)\right) \tag{7}$$

where N_{facets} is the number of facets, S_F is the solar flux, m is the mass of the SO, c is the speed of light, and $\mathcal{A}(i)$ is the area of the i^{th} facet. The unit vector $\boldsymbol{u}_n^I(i)$ is the normal vector pointing outward along the i^{th} surface and $\boldsymbol{u}_{sun}^I$ is the unit vector pointing from the SO to the Sun. Scalars s and d are the fraction of the specular bidirectional reflectance R_s and the diffuse bidirectional reflectance R_d, respectively, where $s + d = 1$. F_0 and ρ are the specular and diffuse reflectance of the facet i at normal incidence, respectively.

As commonly done in aerospace engineering applications (Zanetti, 2019), the direction cosine matrix is used as the attitude matrix representation in this study. The relationship between the vector $\boldsymbol{v}^B$ in the body frame and the vector $\boldsymbol{v}^I$ in the inertial frame is described by the attitude matrix $A(\boldsymbol{q})$ such as

$$\boldsymbol{v}^B = A(\boldsymbol{q})\boldsymbol{v}^I \tag{8}$$

and the attitude matrix can be parameterized in terms of the quaternion as follows:

$$A(\boldsymbol{q}) = I_{3\times 3} - 2q[\boldsymbol{\varrho}\times] + 2[\boldsymbol{\varrho}\times]^2 \tag{9}$$

where

$$[\boldsymbol{a}\times] = \begin{bmatrix} 0 & -a_3 & a_2 \\ a_3 & 0 & -a_1 \\ -a_2 & a_1 & 0 \end{bmatrix} \tag{10}$$

is the skew-symmetric matrix representation of the cross product for a vector $\boldsymbol{a}$. The quaternion dynamic equation is given by

$$\dot{\boldsymbol{q}} = \frac{1}{2}\Omega \cdot \boldsymbol{q} \tag{11}$$

where

$$\Omega = \begin{bmatrix} 0 & \omega_z & -\omega_y & \omega_x \\ -\omega_z & 0 & \omega_x & \omega_y \\ \omega_y & -\omega_x & 0 & \omega_z \\ -\omega_x & -\omega_y & -\omega_z & 0 \end{bmatrix} \tag{12}$$

is the skew-symmetric form of the body rotation about the inertial frame. The angular velocity dynamic equation is expressed as follows:

$$\dot{\boldsymbol{\omega}}^B_{B/I} = J_{SO}^{-1}\left(\boldsymbol{T}^B_{srp} - \left[\boldsymbol{\omega}^B_{B/I}\times\right] J_{SO}\boldsymbol{\omega}^B_{B/I}\right) \tag{13}$$

where J_{SO} is the inertia matrix of the SO and $\boldsymbol{T}^B_{srp}$ is the total torque acting on the SO due to SRP in body frame. The force due to SRP can be assumed to act on the centroid of each surface. Then, the total torque is calculated by

$$\boldsymbol{T}^B_{srp} = m \sum_{i=1}^{N_{facets}} \left[l^B(i)\times\right] A(\boldsymbol{q})\boldsymbol{a}^I_{srp}(i) \tag{14}$$

where $l^B(i)$ is the position vector from the center of the mass of the SO to the geometric center of the i^{th} facet in body frame.

2.2. *Measurement Model*

Angle data in the form of azimuth (az) and elevation (el) are measures used to estimate the states of SO. The angle observation equations are expressed as follows:

$$az = \tan^{-1}\left(\frac{\rho_E}{\rho_N}\right) \tag{15}$$

$$el = \sin^{-1}\left(\frac{\rho_U}{\|\boldsymbol{d}^I\|}\right) \tag{16}$$

where

$$\begin{bmatrix} \rho_E \\ \rho_N \\ \rho_U \end{bmatrix} = \begin{bmatrix} 1 & 0 & 0 \\ 0 & \cos(\frac{\pi}{2}-\lambda) & \sin(\frac{\pi}{2}-\lambda) \\ 0 & -\sin(\frac{\pi}{2}-\lambda) & \cos(\frac{\pi}{2}-\lambda) \end{bmatrix} \begin{bmatrix} \cos(\frac{\pi}{2}+\theta) & \sin(\frac{\pi}{2}+\theta) & 0 \\ -\sin(\frac{\pi}{2}+\theta) & \cos(\frac{\pi}{2}+\theta) & 0 \\ 0 & 0 & 1 \end{bmatrix} \boldsymbol{d}^I \tag{17}$$

where $\boldsymbol{d}^I$ is the position vector from an observer to the SO, $\|\cdot\|$ means the Euclidean norm, θ and λ are the sidereal time and geodetic latitude of the observer, respectively, and $[\rho_E\ \rho_N\ \rho_U]^{\mathrm{T}}$ is the position vector converted from the inertial to the local topocentric East-North-Up coordinates. In this study, light travel time delay is not considered.

Along with the azimuth and elevation, the light curves, which are the time-varying apparent brightness measurements of the SO, are also used. The apparent brightness magnitude measured by the observer is computed by

$$m_{app} = -26.7 - 2.5\log_{10}\left|\sum_{i=1}^{N_{facets}} \frac{f_r(i)\mathcal{A}(i)\left(\boldsymbol{u}^I_n(i)\cdot\boldsymbol{u}^I_{sun}\right)\left(\boldsymbol{u}^I_n(i)\cdot\boldsymbol{u}^I_{obs}\right)}{\|\boldsymbol{d}^I\|^2}\right| \tag{18}$$

where -26.7 is the apparent magnitude of the Sun, $\boldsymbol{u}_{obs}^I$ is the unit vector pointing from the SO to the observer, and $f_r(i)$ is the bidirectional reflectance distribution function (BRDF) for the i^{th} facet. The BRDF models light distribution of a surface due to incident light and it is a function of two directions, one toward the light source and one toward the observer (Linares et al., 2014d; Ashikhmin and Shirley, 2000). The BRDF can be decomposed into a specular component and a diffuse component as follows:

$$f_r(i) = sR_s(i) + dR_d(i) \tag{19}$$

The specular reflectance is mirror-like and the diffuse reflectance is Lambertian which means that light is equally reflected in all directions. These bidirectional reflectances are calculated differently for the various models. In this paper, we use a modified version of the Phong model with a simple form of a non-Lambertian diffuse reflectance (Ashikhmin and Shirley, 2000). Under the flat facet assumption, the specular bidirectional reflectance is given by

$$R_s(i) = \frac{\sqrt{(n_u(i)+1)(n_v(i)+1)}}{8\pi} \frac{\left(\boldsymbol{u}_n^I(i) \cdot \boldsymbol{u}_h^I\right)^{n_u(i)\left(\boldsymbol{u}_u^I(i)\cdot\boldsymbol{u}_h^I\right)^2 + n_v(i)\left(\boldsymbol{u}_v^I(i)\cdot\boldsymbol{u}_h^I\right)^2}}{\boldsymbol{u}_n^I(i)\cdot\boldsymbol{u}_{sun}^I + \boldsymbol{u}_n^I(i)\cdot\boldsymbol{u}_{obs}^I - \left(\boldsymbol{u}_n^I(i)\cdot\boldsymbol{u}_{sun}^I\right)\left(\boldsymbol{u}_n^I(i)\cdot\boldsymbol{u}_{obs}^I\right)} F(i) \tag{20}$$

where $n_u(i)$ and $n_v(i)$ are the anisotropic reflectance properties of the i^{th} surface along the $\boldsymbol{u}_u^B(i)$ and $\boldsymbol{u}_v^B(i)$ directions, respectively. Without loss of functionality, in this study they are assumed to be set equal to each other for the sake of simplicity $(n_u(i) = n_v(i) = n(i))$. Then, Eq. (20) is simplified as follows:

$$R_s(i) = \frac{(n(i)+1)}{8\pi} \frac{\left(\boldsymbol{u}_n^I(i)\cdot\boldsymbol{u}_h^I\right)^{n(i)}}{\boldsymbol{u}_n^I(i)\cdot\boldsymbol{u}_{sun}^I + \boldsymbol{u}_n^I(i)\cdot\boldsymbol{u}_{obs}^I - \left(\boldsymbol{u}_n^I(i)\cdot\boldsymbol{u}_{sun}^I\right)\left(\boldsymbol{u}_n^I(i)\cdot\boldsymbol{u}_{obs}^I\right)} F(i) \tag{21}$$

where $\boldsymbol{u}_h^I$ is the normalized half vector which bisects the angle between $\boldsymbol{u}_{sun}^I$ and $\boldsymbol{u}_{obs}^I$:

$$\boldsymbol{u}_h^I = \frac{\boldsymbol{u}_{sun}^I + \boldsymbol{u}_{obs}^I}{\|\boldsymbol{u}_{sun}^I + \boldsymbol{u}_{obs}^I\|} \tag{22}$$

and the Fresnel reflectance $F(i)$ is approximated as

$$F(i) = F_0(i) + \left(\frac{1}{s} - F_0(i)\right)\left(\boldsymbol{u}_{sun}^I \cdot \boldsymbol{u}_h^I\right) \tag{23}$$

The diffuse bidirectional reflectance is calculated as follows:

$$R_d(i) = \frac{28\rho}{23\pi}(1 - sF_0)\left[1 - \left(1 - \frac{\boldsymbol{u}_n^I(i)\cdot\boldsymbol{u}_{sun}^I}{2}\right)^5\right]\left[1 - \left(1 - \frac{\boldsymbol{u}_n^I(i)\cdot\boldsymbol{u}_{obs}^I}{2}\right)^5\right] \tag{24}$$

The apparent magnitude is measured differently mainly depending on the SO attitude and it has the highest value when the surface normal vector $\boldsymbol{u}_n^I$ and the half vector $\boldsymbol{u}_h^I$ are in the same direction. The various values of apparent magnitude depending on the SO attitude are analyzed in Hinks et al. (2013).

2.3. Filter States

In this paper, it is assumed that the shape of the SO is a cube and each facet of it has the same BRDF surface parameters. The area and mass of the SO are assumed to be known. In addition, the specular reflectance F_0 and diffuse reflectance ρ at normal incidence can be set to be equal to each other because the difference between specular and diffuse reflectance can be expressed by specular s and diffuse fraction parameter d. Thus, the three unique surface parameters to be estimated are n. ρ, d, and the obey the following constraints:

$$n < 0, \quad 0 \leq \rho \leq 1, \quad 0 \leq d \leq 1, \quad s + d = 1$$

Therefore, the state vector utilized is:

$$\boldsymbol{x} = \left[\boldsymbol{q}^{\mathrm{T}} \ \left(\boldsymbol{\omega}_{B/I}^{B}\right)^{\mathrm{T}} \ \left(\boldsymbol{r}^{I}\right)^{\mathrm{T}} \ \left(\boldsymbol{v}^{I}\right)^{\mathrm{T}} \ n \ \rho \ d\right]^{\mathrm{T}} \tag{25}$$

3. Nonlinear Estimation Techniques for Highly Nonlinear Systems

This section presents the three different estimation algorithms used to analyze the problem at hand: particle Gaussian mixture filter with an EM algorithm, truncated interval unscented Kalman filter, and truncated extended Kalman filter.

3.1. Particle Gaussian Mixture Filter with an EM Algorithm

The particle filter (PF) with an EM clustering algorithm for GMMs is proposed in this section. A recursive algorithm is used, i.e. knowledge of the distribution $p(\boldsymbol{x}_{k-1}|\boldsymbol{y}_{k-1})$ at the prior time is assumed and approximated by N identically distributed (i.i.d.) samples $\boldsymbol{x}_{k-1}^{(i)}$ such that

$$p(\boldsymbol{x}_{k-1}|\boldsymbol{y}_{k-1}) \approx \sum_{i=1}^{N} \frac{1}{N} \delta(\boldsymbol{x}_{k-1} - \boldsymbol{x}_{k-1}^{(i)}) \tag{26}$$

where k is an integer that indicates the discrete time step, $\boldsymbol{y}$ is a measurement vector, and $\delta(\cdot)$ is the Dirac delta function. As in the bootstrap particle filter (Arulampalam et al., 2004), a set of samples at the next time step is generated using the Markov transition kernel $p(\boldsymbol{x}_k|\boldsymbol{x}_{k-1})$. Throughout this research, SRP and J_2 are the only perturbations included and additional process noise is neglected. This is a particularly challenging assumption, as particle filters typically rely on process noise to overcome impoverishment.

The next step is to cluster the data into Gaussian mixtures using an EM clustering algorithm. The EM algorithm for GMM approximates the PDF of $\boldsymbol{x}_k$ by combining several Gaussian components having different means, covariance matrices, and weights. With the i.i.d. data set, the likelihood function for the GMM is expressed by

$$p(\boldsymbol{x}_k|\pi, \mu, \Sigma) = \prod_{i=1}^{N} \sum_{j=1}^{K} \pi_j n(\boldsymbol{x}_k^{(i)}|\boldsymbol{\mu}_j, \Sigma_j) \tag{27}$$

where K is a preassigned number of clusters, $n(\boldsymbol{x}|\boldsymbol{\mu}, \Sigma)$ represents the Gaussian PDF with mean $\boldsymbol{\mu}$ and covariance Σ; and $\boldsymbol{\mu}_j$, Σ_j, and π_j are the means, covariance matrices, and weights of the j^{th} Gaussian component. The PDF's normalization and positivity properties lead to the following constraints on the weights:

$$\pi_j \geq 0, \ \forall j \qquad \sum_{j=1}^{K} \pi_j = 1 \tag{28}$$

The goal of the EM clustering algorithm is to maximize the likelihood function with respect to the clustering parameters which are means and covariance matrices of the components, as well as the weights. The algorithm is summarized as follows:

1. Initialize the means $\boldsymbol{\mu}_j$, covariance matrices Σ_j and weights π_j, and evaluate the initial value of the log likelihood.

$$\ln p(\boldsymbol{x}_k|\pi,\mu,\Sigma) = \sum_{i=1}^{N} \ln\left[\sum_{j=1}^{K} \pi_j n(\boldsymbol{x}_k^{(i)}|\boldsymbol{\mu}_j,\Sigma_j)\right] \tag{29}$$

2. (E step) Evaluate the responsibilities using the current clustering parameter values.

$$\gamma(z_j^{(i)}) = p(z_j^{(i)} = 1|\boldsymbol{x}_k^{(i)}) = \frac{\pi_j n(\boldsymbol{x}_k^{(i)}|\boldsymbol{\mu}_j,\Sigma_j)}{\sum_m^K \pi_m n(\boldsymbol{x}_k^{(i)}|\boldsymbol{\mu}_m,\Sigma_m)} \tag{30}$$

where $\gamma(z_j^{(i)})$ is the responsibility of a sample i with respect to a jth Gaussian distribution.

3. (M step) Estimate the new clustering parameters using the current responsibilities to maximize the likelihood. (The following equations are derived in Bishop (2006))

$$\boldsymbol{\mu}_j = \frac{\sum_{i=1}^N \gamma(z_j^{(i)})\boldsymbol{x}_k^{(i)}}{\sum_{i=1}^N \gamma(z_j^{(i)})} \tag{31}$$

$$\boldsymbol{\Sigma}_j = \frac{\sum_{i=1}^N \gamma(z_j^{(i)})(\boldsymbol{x}_k^{(i)} - \boldsymbol{\mu}_j)(\boldsymbol{x}_k^{(i)} - \boldsymbol{\mu}_j)^T}{\sum_{i=1}^N \gamma(z_j^{(i)})} \tag{32}$$

$$\pi_j = \frac{1}{N}\sum_{i=1}^{N} \gamma(z_j^{(i)}) \tag{33}$$

4. Evaluate the value of the log likelihood and check for convergence of it. If the convergence criterion is not satisfied, replace the old clustering parameters with the new ones and return to step 2.

In this paper all components of the GMM are taken with the same covariance matrix, this assumption avoid the GMMs from being too overlapped, while not enforcing hard clustering as in K-means.

Finally, we can incorporate the measurement information by updating the means and covariance matrices of all K components using Kalman measurement update. The mixture weights need to be updated as well using the components likelihood functions. We then draw N i.i.d. samples from the posterior distribution; from these samples, we construct a Bayesian estimate and use them as a starting point for the next iteration. The details of the measurement update and the method to draw N i.i.d. samples from a GMM are explained in Yun and Zanetti (2019).

Two approaches to enforce the surface parameters constraints are evaluated. The first approach is to modify them to unconstrained proxy values. For this study, the same conversion equation used in Wetterer et al. (2013) is applied to convert the surface parameters to the corresponding proxy value and vice versa:

$$p_1 = \ln(n), \quad n = \exp(p_1) \tag{34}$$

$$p_2 = \frac{1}{2}\ln\left(\frac{\rho}{1-\rho}\right), \quad \rho = \frac{1}{2}\left(\tanh(p_2) + 1\right) \tag{35}$$

$$p_3 = \frac{1}{2}\ln\left(\frac{d}{1-d}\right), \quad d = \frac{1}{2}\left(\tanh(p_3) + 1\right) \tag{36}$$

Alternatively, rather than transforming the surface parameters, we can modify the filter to exploit the additional information on the constraints and improve the performance of the filter. In this paper, we use the modified rejection-sampling approach which enforces the constraints by simply discarding the particles violating them in the prediction step. Although the number of total samples will be reduced, it is shown that the algorithm maintains the generic properties of the PF (Papi et al., 2012).

The filter's density, under the assumption of a perfect clustering scheme, converges in probability to the true filter density (Raihan and Chakravorty, 2018). The other two approaches studied are based on the constrained UKF and EKF with the PDF truncation approach, which are computationally cheaper and will be presented in the following two subsections.

3.2. Truncated Interval Unscented Kalman Filter

The UKF is a linear estimator for nonlinear systems which employs statistical linearization of nonlinear functions through a set of sigma points (Lefebvre et al., 2002). The most common schemes to calculate sigma points effectively employs the Gaussian approximation (Julier et al., 2000). The truncated interval unscented Kalman filter (TIUKF) is used in this study to include the inequality constraints on the surface parameters. The TIUKF is composed of two parts: the interval constrained approach which enforces the sigma points interval constraints and the PDF truncation approach which truncates the PDF at the constraint edges (Vachhani et al., 2006; Simon, 2006; Teixeira et al., 2010).

The generic nonlinear dynamics is given by

$$\boldsymbol{x}_{k+1} = \boldsymbol{f}_k(\boldsymbol{x}_k) + \boldsymbol{\nu}_k \tag{37}$$

where k is the time step, $\boldsymbol{x}_k$ is an $n_{\boldsymbol{x}} \times 1$ vector, $\boldsymbol{f}_k$ is some nonlinear function, and the process noise $\boldsymbol{\nu}_k$ is zero-mean white noise, albeit in this application it will be taken as zero. The measurement is

$$\boldsymbol{y}_k = \boldsymbol{h}_k(\boldsymbol{x}_k) + \boldsymbol{\eta}_k \tag{38}$$

where $\boldsymbol{y}_k$ is a measurement vector, $\boldsymbol{h}_k$ is some non-linear function, and $\boldsymbol{\eta}_k$ is the measurement noise consisting of a zero-mean, white sequence with covariance matrix $\boldsymbol{R}_k$, independent from the initial distribution of $\boldsymbol{x}_0$. In addition, assume that the state vector satisfies the interval constraint as follows:

$$\boldsymbol{b}_k \leq \boldsymbol{x}_k \leq \boldsymbol{c}_k \tag{39}$$

where $\boldsymbol{b}_k \in \mathbb{R}^{n_{\boldsymbol{x}}}$ and $\boldsymbol{c}_k \in \mathbb{R}^{n_{\boldsymbol{x}}}$ are known vectors. If the state vector $\boldsymbol{x}_{i,k}$, where $i = 1, \cdots, n_{\boldsymbol{x}}$, is one-sided, we set $\boldsymbol{b}_{i,k} = -\infty$ or $\boldsymbol{c}_{i,k} = \infty$.

Given an $n_{\boldsymbol{x}} \times n_{\boldsymbol{x}}$ error covariance matrix $P^{xx}_{k|k}$, we generate the $2n_{\boldsymbol{x}} + 1$ sigma points $\mathcal{X}_{k|k}$ holding

$$\boldsymbol{b}_k \leq \mathcal{X}_{j,k|k} \leq \boldsymbol{c}_k, \quad j = 0, \cdots, 2n_{\boldsymbol{x}}. \tag{40}$$

To satisfy the inequality constraints, the sigma points are chosen as follows:

$$\mathcal{X}_{k|k} = \hat{\boldsymbol{x}}_{k|k} \mathbb{1}_{1\times(2n_{\boldsymbol{x}}+1)} + \left[\mathbf{0}_{n_{\boldsymbol{x}}\times 1},\ \theta_{1,k}\mathrm{col}_1\left[S_k\right],\ \cdots,\ \theta_{2n_{\boldsymbol{x}},k}\mathrm{col}_{2n_{\boldsymbol{x}}}\left[S_k\right]\right] \tag{41}$$

where $\hat{\boldsymbol{x}}_{k|k}$ is the a posteriori state estimate which is assumed to satisfy the interval constraints at time instant k, $\mathbb{1}_{1\times(2n_{\boldsymbol{x}}+1)}$ is an indicator function,

$$S_k = \left[\left(P^{xx}_{k|k}\right)^{1/2} \ -\left(P^{xx}_{k|k}\right)^{1/2}\right], \tag{42}$$

and

$$\theta_{j,k} = \min\left(\sqrt{n_{\boldsymbol{x}} + \lambda_U},\ \Theta_1,\ \Theta_2\right), \quad \text{for } j = 1, \cdots, 2n_{\boldsymbol{x}} \tag{43}$$

where, for $i = 1, \cdots, n_{\boldsymbol{x}}$,

$$\Theta_1 = \min_{j: S_{(i,j),k} > 0}\left(\infty,\ \frac{c_{i,k} - \hat{\boldsymbol{x}}_{i,k|k}}{S_{(i,j),k}}\right), \quad \Theta_2 = \min_{j: S_{(i,j),k} < 0}\left(\infty,\ \frac{b_{i,k} - \hat{\boldsymbol{x}}_{i,k|k}}{S_{(i,j),k}}\right), \tag{44}$$

and $\lambda_U = \alpha^2\left(n_{\boldsymbol{x}} + \kappa\right) - n_{\boldsymbol{x}}$ is a scaling parameter (Wan and Merwe, 2000). The constant α determines the spread of the sigma points around $\hat{\boldsymbol{x}}_{k|k}$ and it is usually set to a small positive number ($10^{-4} \leq \alpha \leq 1$). κ is a secondary scaling parameter which is usually set to $3 - n_{\boldsymbol{x}}$. Based on the above sigma points, the associated weights are computed as follows:

$$W^m_0 = e_k, \quad W^c_0 = e_k + \left(1 - \alpha^2 + \beta\right) \tag{45}$$

$$W^m_j = W^c_j = d_k\theta_{j,k} + e_k, \quad \text{for } j = 1, \cdots, 2n_{\boldsymbol{x}} \tag{46}$$

where the constant β is used to include prior knowledge of the distribution of $\boldsymbol{x}$, and

$$d_k = \frac{2\lambda_U - 1}{2\left(n_{\boldsymbol{x}} + \lambda_U\right)\left(\sum_{j=1}^{n_{\boldsymbol{x}}}\theta_{j,k} - \left(2n_{\boldsymbol{x}} + 1\right)\sqrt{n_{\boldsymbol{x}} + \lambda_U}\right)} \tag{47}$$

$$e_k = \frac{1}{2\left(n_{\boldsymbol{x}} + \lambda_U\right)} - \frac{2\lambda_U - 1}{2\sqrt{n_{\boldsymbol{x}} + \lambda_U}\left(\sum_{j=1}^{n_{\boldsymbol{x}}}\theta_{j,k} - \left(2n_{\boldsymbol{x}} + 1\right)\sqrt{n_{\boldsymbol{x}} + \lambda_U}\right)} \tag{48}$$

The derivation of the weights equations is described in Vachhani et al. (2006).

Figure 2 illustrates how the sigma points of the TIUKF are chosen compared to the sigma points of the conventional UKF in two dimensional system. When the scaling parameters are $\alpha = 1$, $\beta = 2$, and $\kappa = 1$, and the interval constrains are $b_k = [3\ 2]^{\mathrm{T}}$ and $c_k = [8\ 8]^{\mathrm{T}}$, the mean and covariance matrix of the TIUKF are obtained as follows:

$$\hat{\boldsymbol{x}}_{UKF} = \begin{bmatrix} 4 \\ 4 \end{bmatrix} \Rightarrow \hat{\boldsymbol{x}}_{TIUKF} = \begin{bmatrix} 4.3717 \\ 4.2587 \end{bmatrix} \tag{49}$$

$$\hat{P}^{xx}_{UKF} = \begin{bmatrix} 3 & 0 \\ 0 & 3 \end{bmatrix} \Rightarrow \hat{P}^{xx}_{TIUKF} = \begin{bmatrix} 1.7122 & 0.0962 \\ 0.0962 & 1.8456 \end{bmatrix} \tag{50}$$

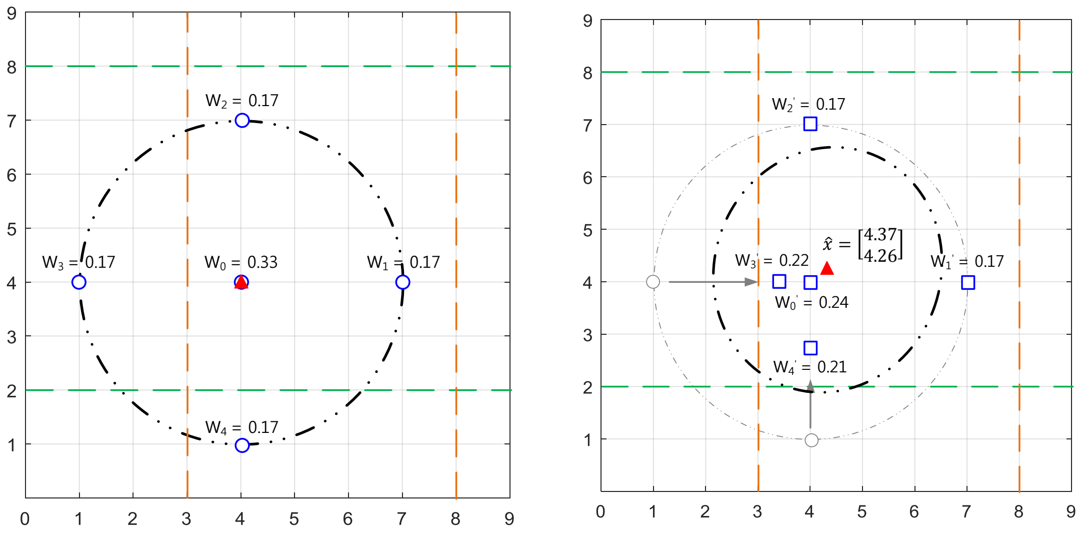

(a) Sigma points and weights of UKF

(b) Sigma points and weights of TIUKF

Figure 2: Comparison of the sigma points and weights in UKF and TIUKF

With the above sigma points, the time update equations are the same as the conventional UKF:

$$\mathcal{X}_{j,k+1|k} = \boldsymbol{f}_k(\mathcal{X}_{j,k|k}), \quad j = 0, \cdots, 2n_{\boldsymbol{x}} \tag{51}$$

$$\hat{\boldsymbol{x}}_{k+1|k} = \sum_{j=0}^{2n_{\boldsymbol{x}}} W_j^m \mathcal{X}_{j,k+1|k} \tag{52}$$

$$P_{k+1|k}^{xx} = \sum_{j=0}^{2n_{\boldsymbol{x}}} W_j^c \left[\mathcal{X}_{j,k+1|k} - \hat{\boldsymbol{x}}_{k+1|k}\right] \left[\mathcal{X}_{j,k+1|k} - \hat{\boldsymbol{x}}_{k+1|k}\right]^{\mathrm{T}} \tag{53}$$

where $\hat{\boldsymbol{x}}_{k+1|k}$ is the a priori state estimate and $P_{k+1|k}^{xx}$ is the a priori state estimation error covariance. With the propagated estimates $\hat{\boldsymbol{x}}_{k+1|k}$ and $P_{k+1|k}^{xx}$, a new set of sigma points $\mathcal{X}_{k+1|k}$ of the TIUKF which satisfy the interval constraints and the corresponding weights are recalculated. Then, the measurement update equations are expressed as follows:

$$\mathcal{Y}_{j,k+1|k} = \boldsymbol{h}_{k+1}(\mathcal{X}_{j,k+1|k}), \quad j = 0, \cdots, 2n_{\boldsymbol{x}} \tag{54}$$

$$\hat{\boldsymbol{y}}_{k+1} = \sum_{j=0}^{2n_{\boldsymbol{x}}} W_j^m \mathcal{Y}_{j,k+1|k} \tag{55}$$

$$P_{k+1|k}^{yy} = \sum_{j=0}^{2n_{\boldsymbol{x}}} W_j^c \left[\mathcal{Y}_{j,k+1|k} - \hat{\boldsymbol{y}}_{k+1}\right] \left[\mathcal{Y}_{j,k+1|k} - \hat{\boldsymbol{y}}_{k+1}\right]^{\mathrm{T}} + \boldsymbol{R}_k \tag{56}$$

$$P_{k+1|k}^{xy} = \sum_{j=0}^{2n_{\boldsymbol{x}}} W_j^c \left[\mathcal{X}_{j,k+1|k} - \hat{\boldsymbol{x}}_{k+1|k}\right] \left[\mathcal{Y}_{j,k+1|k} - \hat{\boldsymbol{y}}_{k+1}\right]^{\mathrm{T}} \tag{57}$$

$$\hat{\boldsymbol{x}}_{k+1|k+1} = \hat{\boldsymbol{x}}_{k+1|k} + P_{k+1|k}^{xy} \left(P_{k+1|k}^{yy}\right)^{-1} \left(\boldsymbol{y}_{k+1} - \hat{\boldsymbol{y}}_{k+1}\right) \tag{58}$$

$$P_{k+1|k+1}^{xx} = P_{k+1|k}^{xx} - P_{k+1|k}^{xy} \left(P_{k+1|k}^{yy}\right)^{-1} \left(P_{k+1|k}^{xy}\right)^{\mathrm{T}} \tag{59}$$

where $P^{xx}_{k+1|k+1}$ is the a posteriori state estimation error covariance, $P^{yy}_{k+1|k}$ is the measurement residual covariance, and $P^{xy}_{k+1|k}$ is the cross covariance.

We then perform the PDF truncation process. The constrained state estimate is the mean of the truncated Gaussian PDF at the constraint edges. The state estimate is normalized in a way that its components are statistically independent of each other to reduce computational effort to determine the truncated PDF. Then the part of the Gaussian PDF which is outside of the constraints is removed. After all the constraints are sequentially applied to the corresponding component, we then revert the normalization process to obtain the constrained state estimate. The details of the algorithm are explained in Simon (2006) and Simon and Simon (2010).

3.3. Truncated Extended Kalman Filter

The EKF is a nonlinear approximation of the Kalman filter that can be applied to nonlinear systems using the same Kalman filtering framework. Given the system model, Eq. (37) and Eq. (38), the time update equations are described as follows:

$$\hat{\boldsymbol{x}}_{k+1|k} = \boldsymbol{f}_k(\hat{\boldsymbol{x}}_{k|k}) \tag{60}$$

$$P^{xx}_{k+1|k} = F_k P^{xx}_{k|k} F_k^{\mathrm{T}} \tag{61}$$

$$F_k = \left.\frac{\partial \boldsymbol{f}_k(\boldsymbol{x})}{\partial \boldsymbol{x}}\right|_{\boldsymbol{x}=\hat{\boldsymbol{x}}_{k|k}} \tag{62}$$

where F_k is the Jacobian of the dynamics evaluated at the posterior mean $\hat{\boldsymbol{x}}_{k|k}$. The measurement update equations are:

$$\hat{\boldsymbol{x}}_{k+1|k+1} = \hat{\boldsymbol{x}}_{k+1|k} + K_{k+1}\left(\boldsymbol{y}_{k+1} - \boldsymbol{h}_{k+1}(\hat{\boldsymbol{x}}_{k+1|k})\right) \tag{63}$$

$$P^{xx}_{k+1|k+1} = P^{xx}_{k+1|k} - K_{k+1} W_{k+1} K^{\mathrm{T}}_{k+1} \tag{64}$$

$$K_{k+1} = P^{xx}_{k+1|k} H^{\mathrm{T}}_{k+1} W^{-1}_{k+1} \tag{65}$$

$$W_{k+1} = H_{k+1} P^{xx}_{k+1|k} H^{\mathrm{T}}_{k+1} + R_{k+1} \tag{66}$$

$$H_{k+1} = \left.\frac{\partial \boldsymbol{h}_{k+1}(\boldsymbol{x})}{\partial \boldsymbol{x}}\right|_{\boldsymbol{x}=\hat{\boldsymbol{x}}_{k+1|k}} \tag{67}$$

where H_{k+1} is the Jacobian of the measurement evaluated at the prior mean $\hat{\boldsymbol{x}}_{k+1|k}$, K_{k+1} is the Kalman gain, and W_{k+1} is the measurement residual covariance. The PDF truncation step which is explained in the previous subsection is then applied to the truncated extended Kalman filter (TEKF) (Simon and Simon, 2010).

Despite of the additional information on the constraints, the severe nonlinearities of the system can lead to divergence of the TEKF. For example, the approximation error caused by truncating the nonlinear functions to the first-order (e.g. Eq. (62) and Eq. (67)) can be significant. It is well-known that when measurement noise is small while the a priori uncertainty of the state estimate is relatively large, nonlinear effects can become very significant (Maybeck, 1982; Zanetti et al., 2010).

To analyze nonlinear effects on the measurement update in detail, a Gaussian second-order filter is considered which includes the second-order terms in the Taylor series expansion (Maybeck, 1982). The Kalman gain and measurement residual covariance in the Gaussian second-order filter are expressed as follows:

$$K_{k+1}^{2nd} = P_{k+1|k}^{xx} H_{k+1}^{\mathrm{T}} \left(W_{k+1}^{2nd}\right)^{-1} \tag{68}$$

$$W_{k+1}^{2nd} = H_{k+1} P_{k+1|k}^{xx} H_{k+1}^{\mathrm{T}} + R_{k+1} + B_{k+1} \tag{69}$$

where matrix B_{k+1} is the contribution of the second-order effects and the ij^{th} component of B_{k+1}, under the Gaussian approximation, is given by

$$B_{ij,k+1} = \frac{1}{2} \operatorname{trace} \left(\left. \frac{\partial^2 \boldsymbol{h}_{i,k+1}(\boldsymbol{x})}{\partial \boldsymbol{x} \partial \boldsymbol{x}^{\mathrm{T}}} \right|_{\boldsymbol{x}=\hat{\boldsymbol{x}}_{k+1|k}} P_{k+1|k}^{xx} \left. \frac{\partial^2 \boldsymbol{h}_{j,k+1}(\boldsymbol{x})}{\partial \boldsymbol{x} \partial \boldsymbol{x}^{\mathrm{T}}} \right|_{\boldsymbol{x}=\hat{\boldsymbol{x}}_{k+1|k}} P_{k+1|k}^{xx} \right) \tag{70}$$

where $\boldsymbol{h}_{i,k+1}$ is the i-th component of $\boldsymbol{h}_{k+1}(\boldsymbol{x}_{k+1})$. Comparing the measurement residual covariance for the EKF in Eq. (66) with the measurement residual covariance for the Gaussian second-order filter in Eq. (69) and observed the Gaussian second-order filter gain is smaller than the standard EKF gain when the contribution of the second-order term is significant. Consequently, the state estimation error covariance (Eq. (64)) of the standard EKF decreases more quickly than the actual state error covariance when the contribution of the second-order term is not negligible.

The Gaussian second-order filter is rarely used in practice due to its reliance on the Gaussian approximation, an alternative method to compensate for the high-order effects that allows for tuning are implemented in this paper: Lear's underweighting method (Zanetti et al., 2010). Lear's approach to underweighting the measurement is to add a percentage of the a priori estimation error covariance to the measurement residual covariance:

$$W_{k+1}^{U.W} = H_{k+1} P_{k+1|k}^{xx} H_{k+1}^{\mathrm{T}} + R_{k+1} + \beta_{UW} H_{k+1} P_{k+1|k}^{xx} H_{k+1}^{\mathrm{T}} \tag{71}$$

where β_{UW} is a tuning parameter. The additional term, $\beta_{UW} H_{k+1} P_{k+1|k}^{xx} H_{k+1}^{\mathrm{T}}$, in the measurement residual covariance decreases the Kalman gain, thus reducing the state estimate and a posteriori state estimation error covariance update.

Another approach to make the filter more robust in the presence of high uncertainty and nonlinearities is the consider Kalman filter (Woodbury and Junkins, 2010). The effects of highly nonlinear states of the system can be "considered" only, meaning the states are not updated in the filter. In other words, we only update the state estimates which are not highly nonlinear and the corresponding error covariance based on the uncertainty of the highly nonlinear states. The consider Kalman filter algorithm and derivation are explained in Woodbury and Junkins (2010). In this paper, both methods are applied to the TEKF only when the contribution of the a priori estimated state uncertainty to the residual covariance is much larger than the measurement noise covariance, i.e. $H_{k+1} P_{k+1|k}^{xx} H_{k+1}^{\mathrm{T}} \gg R_{k+1}$, which is a strong indicator that nonlinear effects might become important (Zanetti et al., 2010).

4. Numerical Results

For the state estimation problem described in section 2, we adopted the scenario used in Wetterer et al. (2013) to investigate the divergence and accuracy achievable by recursive estimators, i.e. non-batch. Wetterer et al. (2013)

suggests divergence is due to information dilution, as the available data is scarce and not used in the most appropriate way. We concur with this analysis in that information dilution coupled with severe nonlinearities causes divergence in the UKF. However, information dilution alone is not responsible for divergence as a linear system does not exhibit divergence. The numerical results in this section show that it is possible to design recursive estimators for this problem that do not diverge and that improves the accuracy of all states. It is not only possible with sophisticated sequential Monte Carlo methods, but also with an UKF or even an EKF when appropriate precautions are taken.

In the simulation, a SO is in a geosynchronous orbit with the following orbital elements: $a = 42,364.16932$ km, $e = 0$, $i = 30°$, $M_0 = 91°$, and $\omega = \Omega = 0$. The simulation epoch is 15-March-2010 at 04:00:00 UT and the SO does not pass through the shadow of the Earth during the simulation time. The shape of the SO is a cube with side length 1m and a mass of 2kg and it is assumed that there is no self shadowing in the model. Apparent brightness magnitude and angle measurements are simulated using a ground station located at the top of Haleakala in Maui (latitude $= 20.71°$, longitude $= -156.26°$, and altitude $= 3.5086$km). Measurements are corrupted by additive zero-mean Gaussian white noise with standard deviations of 0.1 for the brightness magnitude and 10 arc-seconds on the azimuth and elevation observation. Both measurements are available every 2 seconds for two hours. The changes we made in this simulation scenario with respect to Wetterer et al. (2013) are that (1) we used the azimuth and elevation observations for angle data instead of right ascension and declination observation and (2) we omitted thermal radiation pressure (TRP) in the dynamics as it did not change the results appreciably. The details of the initial truth state, the initial estimated state, and the initial uncertainty are listed in Table 1. Note that the goal of this study is to estimate attitude, attitude rate, and surface parameters simultaneously, and we do so using the initial conditions highlighted in Wetterer et al. (2013) that include an initial attitude uncertainty of 10 degrees (3σ) and that cause their UKF design to diverge. This is a challenging scenario as all surfaces of the SO are assumed to have the same parameters, hence differnt surfaces are indistinguishable from one another and very large initial attitude errors cannot be resolved. Other studies, including Linares et al. (2014a); Coder et al. (2018a) assume known surface parameters with different values for each facet. Under those conditions, a particle filter is able to resolve initial orientation uncertainties much larger than 10 degrees.

The first goal is to investigate whether information dilution alone can cause divergence, or if a nonlinear filter can be successfully applied to this problem. Many nonlinear algorithms such as various flavors of the particle filter as well as PGMF from Raihan and Chakravorty (2018) and the sequential Monte Carlo filter from Yun and Zanetti (2019) were used and they all diverged. The UKF also diverges. These failures are due to the high nonlinearities of the light-curve data combined with the absence of process noise. Divergence is not an intrinsic property of the system, as the modified PGMF algorithm proposed here, named PFGMM1, is able to prevent the divergence of the state. Figure 3 shows the position, attitude, and surface parameter errors with the corresponding 3σ predictions when PFGMM1 is used. Notice that proxy values are used in order to estimate the surface parameter without any constraint on their values. All errors are consistent with the uncertainties, meaning that the filter does not diverge. From the analysis, it is shown that it is the severe nonlinearities coupled with the weak observability of the system that leads to divergence, not information dilution. The PFGMM uses 3 clusters with 10,000 particles and for this and all subsequent filters the

State	**Initial Truth**	**Initial Estimate**	**Uncertainty** (1σ)
$\boldsymbol{q}$	0.754	0.695	3.33 deg
	0.133	0.134	
	0.000	0.010	
	0.643	0.706	
$\boldsymbol{\omega}_{B/I}^{B}$ (rad/s)	0.00200	0.00212	1.16×10^{-4}
	-0.00100	-0.00106	
	0.00500	0.00506	
$\boldsymbol{r}^{I}$ (km)	-739.4	-789.4	100
	36682.9	36732.9	
	21178.9	21278.9	
$\boldsymbol{v}^{I}$ (km/s)	-3.0669	-3.0169	0.10
	-0.0464	0.0536	
	-0.0268	-0.0768	
n	150	120	30
ρ	0.40	0.10	0.30
d	0.70	1.00	0.30

Table 1: Initial conditions

modified Rodrigues parameters (MRPs) are used to define the local error for the attitude estimation.

The simulation is conducted with the five nonlinear filters described in the previous section: (1) the particle filter with Gaussian mixture models (PFGMM) without the constraint information (PFGMM1), (2) the PFGMM with the constraint information (PFGMM2), (3) the TIUKF, (4) the TEKF with underweighting (TEKF1), and (5) the TEKF with considering parameters (TEKF2).

The introduction of proxy surface parameters, while making the state space unconstrained, adds more nonlinearities to the systems. Alternatively, the constraint can be used as additional information in the modified rejection-sampling algorithm, we denote this filter as PFGMM2. The time history of the state errors and respective 3σ predicted performance when using the PFGMM2 with the modified rejection-sampling approach is depicted in Figure 4. Since the constraint information is added to the estimator, it can be seen that the PFGMM2 has the better performance than the PFGMM1.

The two nonlinear filter proposed (PFGMM1 and PFGMM2) establish that information dilution due to few measurements and many estimated quantities does not necessarily cause filter divergence, and that treating constraints as source of information improves the performance of the filter. The next objective of this investigation is to design a consistent linear estimator, i.e. Kalman filter, which, while producing less accurate estimates than the nonlinear filters above, still produces a consistent, non-diverging solution. The algorithms used are the modifications of the UKF and EKF described in the previous sections.

The TIUKF uses the following tuning parameters: $\alpha = 0.8$, $\beta = 3$, and $\kappa = 3$, for its sigma points spread. The underweighting tuning parameter for the TEKF with underweighting approach (denoted as TEKF1) is $\beta_{UW} = 2.0$. The third and last linear estimator considered is the TEKF with considering parameters (denoted as TEKF2) which treats the surface parameters (since they are highly nonlinear states in the system) as considered states when high nonlinearities are detected. High nonlinearities are declared when $H_{k+1}P^{xx}_{k+1|k}H^{\mathrm{T}}_{k+1} > 3R_{k+1}$ in the brightness magnitude measurement only, as it is the nonlinear measurement that causes divergence.

The simulation results of the three linear filters are shown in Figure 5 to Figure 7. Comparing the error and covariance of all the cases, the performance of those filters is comparable to that of the PFGMMs, yet at a reduced computational cost. Based on the criterion, $H_{k+1}P^{xx}_{k+1|k}H^{\mathrm{T}}_{k+1} > 3R_{k+1}$, the TEKF1 used the underweighting parameter as follows: $\beta_{UW} = 2.0$ for $t \leq 16$ and $\beta_{UW} = 0$ for $t > 16$, where t is the simulation time. With the same criterion, the TEKF2 considers surface parameters when $t \leq 48$ and estimates all the states for the rest of the time. Since the PDF truncation step was performed in the TEKF with the methods to compensate for the high-order effects, the uncertainties of the surface parameters and associated states (i.e. attitude) eventually converge to slightly smaller values than those of the PFGMM1.

Table 2 lists the time-averaged root mean square error (RMSE) for a single simulation. The best performance is obtained with the PFGMM2 when comparing the time-averaged RMSE. In terms of the RMS attitude, angular velocity, and parameter errors, the TEKFs have the better performance than the PFGMM1, which indicates it is possible to improve the PFGMM by increasing the number of particles and clusters. While an increases in the number of particles and clusters might improve the PFGMM, such an increase would increase the computational cost substantially. The computation time for filtering run in MATLAB on a 3.2 GHz hexa-core Windows operation system is also presented in Table 2. In terms of computation time, the TEKFs are the best performers while retaining roughly the same accuracy as the PFGMMs.

Filter	Time-averaged RMSE					Computation time (s)
	Position (m)	Velocity (m/s)	Attitude (deg)	Angular velocity (deg/hr)	Parameter	
PFGMM1	26383.9	22.3130	2.4399	19.9157	8.7214	4090.9011
PFGMM2	22208.3	15.6344	0.7056	7.6407	8.0329	4292.7190
TIUKF	45548.6	21.1789	3.0219	46.9340	10.1084	158.0590
TEKF1	33062.5	22.9153	1.1209	9.1540	8.4212	127.8666
TEKF2	29865.8	22.3357	0.7939	8.9834	8.5570	127.8417

Table 2: RMSE for a single simulation

As results from single runs cannot definitively assess the performance of a stochastic estimator, a Monte Carlo analysis is performed with 100 simulations to compare the performance of the five filters based on the RMSE and the noncredibility index (NCI) (Li and Zhao, 2006). The RMSE is calculated from the true and estimated states at each time k for each Monte Carlo simulation. The NCI is expressed as

$$\mathrm{NCI}_k = \frac{1}{M}\sum_{j=1}^{M}\Big[10\log_{10}\Big((\boldsymbol{x}_k^j-\boldsymbol{\mu}_k^j)^{\mathrm{T}}(\boldsymbol{P}_k^j)^{-1}(\boldsymbol{x}_k^j-\boldsymbol{\mu}_k^j)\Big)-10\log_{10}\Big((\boldsymbol{x}_k^j-\boldsymbol{\mu}_k^j)^{\mathrm{T}}\boldsymbol{\Sigma}_k^{-1}(\boldsymbol{x}_k^j-\boldsymbol{\mu}_k^j)\Big)\Big] \tag{72}$$

where M is the number of Monte Carlo simulations, $\boldsymbol{x}_k^j$ are the true states, $\boldsymbol{\mu}_k^j$ are the estimated states, $\boldsymbol{P}_k^j$ are the filter's error covariance matrix of the j-th Monte Carlo run, and $\boldsymbol{\Sigma}_k$ is the ensemble error covariance matrix of the estimates at time k computed from the Monte Carlo samples. The NCI evaluates the difference between the ideal error covariance matrix $\boldsymbol{\Sigma}_k$ and the estimated error covariance matrix $\boldsymbol{P}_k$. The NCI metric is a geometric average of 10 times the logarithm of the normalized estimation error squared (NEES) ratio; it is a balanced measure of the consistency of the five estimators. When the difference between $\boldsymbol{\Sigma}_k$ and $\boldsymbol{P}_k$ is small, the NCI value should be zero or nearly zero at all times (Li and Zhao, 2006).

Figure 8 to Figure 10 display the time history of the RMS position, velocity, attitude, angular velocity, and parameter errors of the 100 simulations. The time-averaged value of the RMSE of all the filters are listed in Table 3. The surface parameters of the highly nonlinear light curve measurements are associated with the attitude and angular velocity. It is shown in the figures that the results of the RMS attitude, angular velocity, and surface parameter (ρ and d) errors are highly correlated to each other. The best performance is obtained with the PFGMM2. The results also show that although the performance of the TEKF1 and PFGMM2 are comparable, the TEKF2 has the worst performance among the five filters. In terms of the RMS position, velocity, and surface parameter (n) errors, the performances of the TIUKF and PFGMM2 are comparable. However, the RMS attitude, angular velocity, and surface parameter (ρ and d) errors of the TIUKF are higher than those of any filters, which means the TIUKF is adversely affected by the severe nonlinearities of the system. On the other hand, the RMS attitude, angular velocity, and surface parameter errors of the PFGMM1 which does not use the constraint information are comparable to the PFGMM2 while the RMS position and velocity errors of the PFGMM1 are higher than those of any filters.

The consistency test result of each filter represented by the absolute NCI value is shown in Figure 11. In this figure, the NCI values of the PFGMM1 and PFGMM2 are smaller than those of other linear filters and they approach to zero as time passes. The absolute NCI value of the TEKF1 is smaller than that of the TEKF2, which means that Lear's underweighting method is more effective to compensate the nonlinear effects of this system than considering the surface parameters. Moreover, the figure shows that the TIUKF is unsuitable for such a highly nonlinear system. The average computation time per filtering run as well as the time-averaged absolute NCI value are listed in Table 3.

5. Conclusions

This paper presents a detailed study of the estimation of the translational and rotational states of near-geosynchronous objects from bearing angles and light curve data. Three parameters of the highly nonlinear light curve measurements

Filter	Time-averaged RMSE					NCI	Computation time (s/simulation)
	Position (m)	Velocity (m/s)	Attitude (deg)	Angular velocity (deg/hr)	Parameter		
PFGMM1	10473.0	13.3760	3.5661	39.8182	8.9694	6.0991	3886.9418
PFGMM2	6058.0	10.5164	1.8168	20.3907	6.1568	4.6129	3724.6250
TIUKF	6128.7	10.2885	12.9220	124.8847	8.6949	14.5863	120.7671
TEKF1	6768.3	11.2232	2.5504	26.9194	10.3177	11.8965	114.7027
TEKF2	10330.0	13.0897	11.9788	86.2043	18.0175	15.5414	112.6375

Table 3: RMSE for 100 Monte Carlo simulations

are also estimated. The high nonlinearity and weak observability of the system makes this problem particularly challenging for recursing filtering algorithms. This fact is exacerbated by the absence of process noise, which is typically needed to overcome particle impoverishment in particle filters.

A novel approach to nonlinear estimation combining particle filters and Gaussian sum filters using an expectation-maximization clustering method is proposed. The advantage of this algorithm is that the use of soft clustering gives a more accurate Gaussian mixture model representation of the prior probability density function over existing related approaches. The soft-clustering approach allows the filter to converge, while a similar existing algorithm using K-means clustering diverges under the conditions of the example studied. The soft clustering works in a way that each point is assigned to all the clusters with different weights or probabilities, thus obtaining the proper covariance of the components. By designing a consitent filter with the same members of the state space and same measurements, it is shown that dilution of information is not a cause of divergence per-se, rather divergence of prior approaches are due to the severe nonlinearities of the system coupled with large initial uncertainties and weak observability.

Finally, three linear estimators were designed and shown to provide good performance. The truncated interval unscented Kalman filter uses the constraint information in the time and measurement update steps and truncates the probability density function after the measurement update. The truncated extended Kalman filter includes not only the probability density function truncation approach but also two extra methods to compensate nonlinear effects.

Acknowledgment

This work was sponsored in part by the U.S. Air Force Office of Scientific Research under grant number FA9550-18-1-0351.

References

Arulampalam, S., Gordon, N., Ristic, B., 2004. Beyond the Kalman Filter: Particle Filters for Tracking Applications Partical Filters for Tracking Applications. Artech House.

Ashikhmin, M., Shirley, P., 2000. An anisotropic phong light reflection model. Journal of Graphics Tools 5, 25–32. doi: 10.1080/10867651.2000.10487522.

Bishop, C., 2006. Pattern Recognition and Machine Learning. Springer-Verlag, New York, NY. pp. 430-441.

Coder, R.D., Holzinger, M.J., Linares, R., 2018a. Three-degree-of-freedom estimation of agile space objects using marginalized particle filters. Journal of Guidance, Control, and Dynamics 41, 388–400. doi: 10.2514/1.G001980.

Coder, R.D., Wetterer, C.J., Hamada, K.M., Holzinger, M.J., Jah, M.K., 2018b. Inferring active control mode of the hubble space telescope using unresolved imagery. Journal of Guidance, Control, and Dynamics 41, 164–170. doi: 10.2514/1.G002223.

Dianetti, A.D., Weisman, R., Crassidis, J.L., 2018. Observability analysis for improved space object characterization. Journal of Guidance, Control, and Dynamics 41, 137–148. doi: 10.2514/1.G002229.

Fan, S., Frueh, C., 2019. A direct light curve inversion scheme in the presence of measurement noise. The Journal of the Astronautical Sciences , 1–22doi: 10.1007/s40295-019-00190-3.

Fraiture, L., 1986. The Information Dilution Theorem. ESA Journal 10, 381–386.

Hinks, J.C., Linares, R., Crassidis, J.L., 2013. Attitude observability from light curve measurements. AIAA Guidance, Navigation, and Control (GNC) Conference doi: 10.2514/6.2013-5005.

Julier, S., Uhlmann, J., Durrant-Whyte, H.F., 2000. A new method for the nonlinear transformation of means and covariances in filters and estimators. IEEE Transactions on Automatic Control 45, 477–482. doi: 10.1109/9.847726.

Kelecy, T., Jah, M., DeMars, K., 2012. Application of a multiple hypothesis filter to near geo high area-to-mass ratio space objects state estimation. Acta Astronautica 81, 435–444. doi: 10.1016/j.actaastro.2012.08.006.

Lefebvre, T., Bruyninckx, H., Schutter, J.D., 2002. Comment on “A New Method for the Nonlinear Transformation of Means and Covariances in Filters and Estimators”. IEEE Transactions on Automatic Control 47, 1406–1408. Doi: 10.1109/TAC.2002.800742.

Li, X.R., Zhao, Z., 2006. Measuring estimator’s credibility: Noncredibility index, in: 2006 9th International Conference on Information Fusion (FUSION).

Linares, R., Crassidis, J.L., 2018. Space-object shape inversion via adaptive hamiltonian markov chain monte carlo. Journal of Guidance, Control, and Dynamics 41, 47–58. doi: 10.2514/1.G002296.

Linares, R., Crassidis, J.L., Jah, M.K., 2014a. Particle filtering light curve based attitude estimation for non-resolved space objects. Proceedings of the AAS/AIAA Spaceflight Mechanics Meeting 152, 119–130. AAS 14-210.

Linares, R., Crassidis, J.L., Jah, M.K., 2014b. Space object classification and characterization via multiple model adaptive estimation, in: 17th International Conference on Information Fusion (FUSION).

Linares, R., Jah, M.K., Crassidis, J.L., Leve, F.A., Kelecy, T., 2014c. Astrometric and photometric data fusion for inactive space object mass and area estimation. Acta Astronautica 99, 1–15. doi: 10.1016/j.actaastro.2013.10.018.

Linares, R., Jah, M.K., Crassidis, J.L., Nebelecky, C.K., 2014d. Space object shape characterization and tracking using light curve and angles data. Journal of Guidance, Control, and Dynamics 37, 13–25. doi: 10.2514/1.62986.

Linares, R., Leve, F.A., Jah, M.K., Crassidis, J.L., 2012. Space object mass-specific inertia matrix estimation from photometric data. Advances in the Astronautical Sciences 144, 41–54.

Linares, R., Shoemaker, M., Walker, A., Mehta, P.M., Palmer, D.M., Thompsonk, D.C., Koller, J., Crassidis, J.L., 2013. Photometric data from non-resolved objects for space object characterization and improved atmospheric modeling. Advanced Maui Optical and Space Surveillance Technologies Conference 1, 32.

Mallik, V., Jah, M.K., 2019. Reconciling space object observed and solar pressure albedo-areas via astrometric and photometric data fusion. Advances in Space Research 63, 404–416. doi: 10.1016/j.asr.2018.08.005.

Maybeck, P.S., 1982. Stochastic Models, Estimation, and Control, Volume 2. Academic Press, New York, NY.

McMahon, J.W., Scheeres, D.J., 2015. Improving space object catalog maintenance through advances in solar radiation pressure modeling. Journal of Guidance, Control, and Dynamics 38, 1366–1380. doi: 10.2514/1.G000666.

Papi, F., Podt, M., Boers, Y., Battistello, G., Ulmke, M., 2012. On constraints exploitation for particle filtering based target tracking. 15th International Conference on Information Fusion , 455–462.

Raihan, D., Chakravorty, S., 2018. Particle gaussian mixture filters-i. Automatica 98, 331–340. doi: 10.1016/j.automatica.2018.07.023.

Rapoport, I., Bar-Itzhack, I.Y., 2001. On the information dilution theorem and its application to attitude determination. The Journal of the Astronautical Sciences 49, 489–508. ISSN: 0021-9142.

Richardson, M., Kelecy, T., Stauch, J., Wetterer, C.J., Chow, C., 2019. Mass estimation through fusion of astrometric and photometric data with applications to orbital debris characterization. Proceedings of the AAS/AIAA Spaceflight Mechanics Meeting 168, 2209–2227. AAS 19-268.

Schmidt, S.F., 1966. Application of state-space methods to navigation problems. Advances in Control Systems 3, 293–340. doi: 10.1016/B978-1-4831-6716-9.50011-4.

Simon, D., 2006. Optimal State Estimation: Kalman, H-infinity, and Nonlinear Approaches. John Wiley and Sons, New Jersey, NJ. pp. 212-223, doi: 10.1002/0470045345.

Simon, D., Simon, D.L., 2010. Constrained kalman filtering via density function truncation for turbofan engine health estimation. International Journal of Systems Science 41, 159–171. doi: 10.1080/00207720903042970.

Teixeira, B.O.S., Tôrres, L.A.B., Aguirre, L.A., Bernstein, D.S., 2010. On unscented kalman filtering with state interval constraints. Journal of Process Control 20, 45–57. doi: 10.1016/j.jprocont.2009.10.007.

Vachhani, P., Narasimhan, S., Rengaswamy, R., 2006. Robust and reliable estimation via unscented recursive nonlinear dynamic data reconciliation. Journal of Process Control 16, 1075–1086. doi: 10.1016/j.jprocont.2006.07.002.

Wan, E.A., Merwe, R.V.D., 2000. The unscented kalman filter for nonlinear estimation, in: Proceedings of the IEEE 2000 Adaptive Systems for Signal Processing, Communications, and Control Symposium. doi: 10.1109/ASSPCC.2000.882463.

Wetterer, C.J., Chow, C.C., Crassidis, J.L., Linares, R., Jah, M.K., 2013. Simultaneous position, velocity, attitude, angular rates, and surface parameter estimation using astrometric and photometric observations. Proceedings of the 16th International Conference on Information Fusion , 997–1004.

Wetterer, C.J., Hunt, B., Hamada, K., Crassidis, J.L., Kervin, P., 2014. Shape, surface parameter, and attitude profile estimation using a multiple hypothesis unscented kalman filter. Proceedings of the AAS/AIAA Spaceflight Mechanics Meeting 152, 1475–1484. AAS 14-303.

Wetterer, C.J., Jah, M.K., 2009. Attitude estimation from light curves. Journal of Guidance, Control, and Dynamics 32, 1648–1651. doi: 10.2514/1.44254.

Woodbury, D.P., Junkins, J.L., 2010. On the consider kalman filter. AIAA Guidance, Navigation, and Control Conference Paper No. AIAA 2010-7752.

Yun, S., Zanetti, R., 2019. Sequential monte carlo filtering with gaussian mixture sampling. Journal of Guidance, Control, and Dynamics 42, 2069–2077. doi: 10.2514/1.G004403.

Zanetti, R., 2019. Rotations, transformations, left quaternions, right quaternions? The Journal of the Astronautical Sciences 66, 361–381. doi: 10.1007/s40295-018-00151-2.

Zanetti, R., DeMars, K.J., Bishop, R.H., 2010. Underweighting nonlinear measurements. Journal of Guidance, Control, and Dynamics 33, 1670–1675. doi: 10.2514/1.50596.

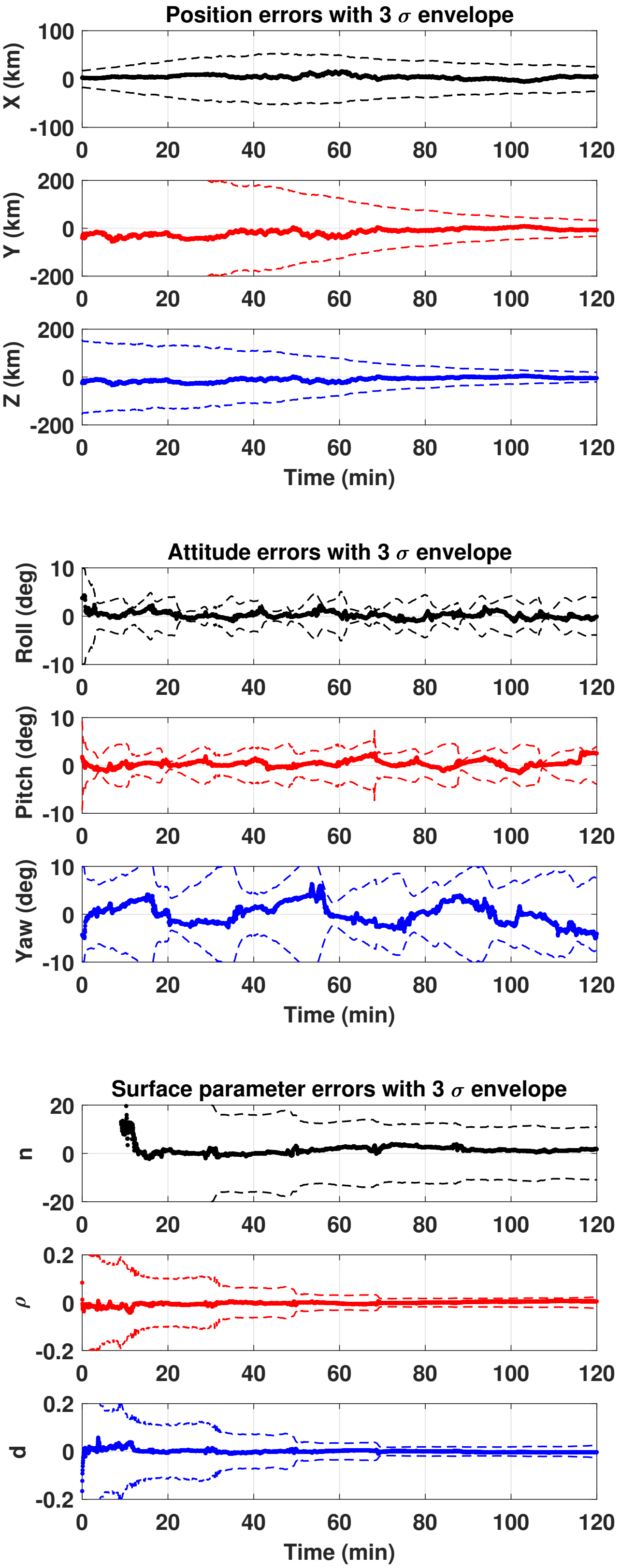

Figure 3: Position, attitude, and surface parameter errors with the PFGMM without the constraint information

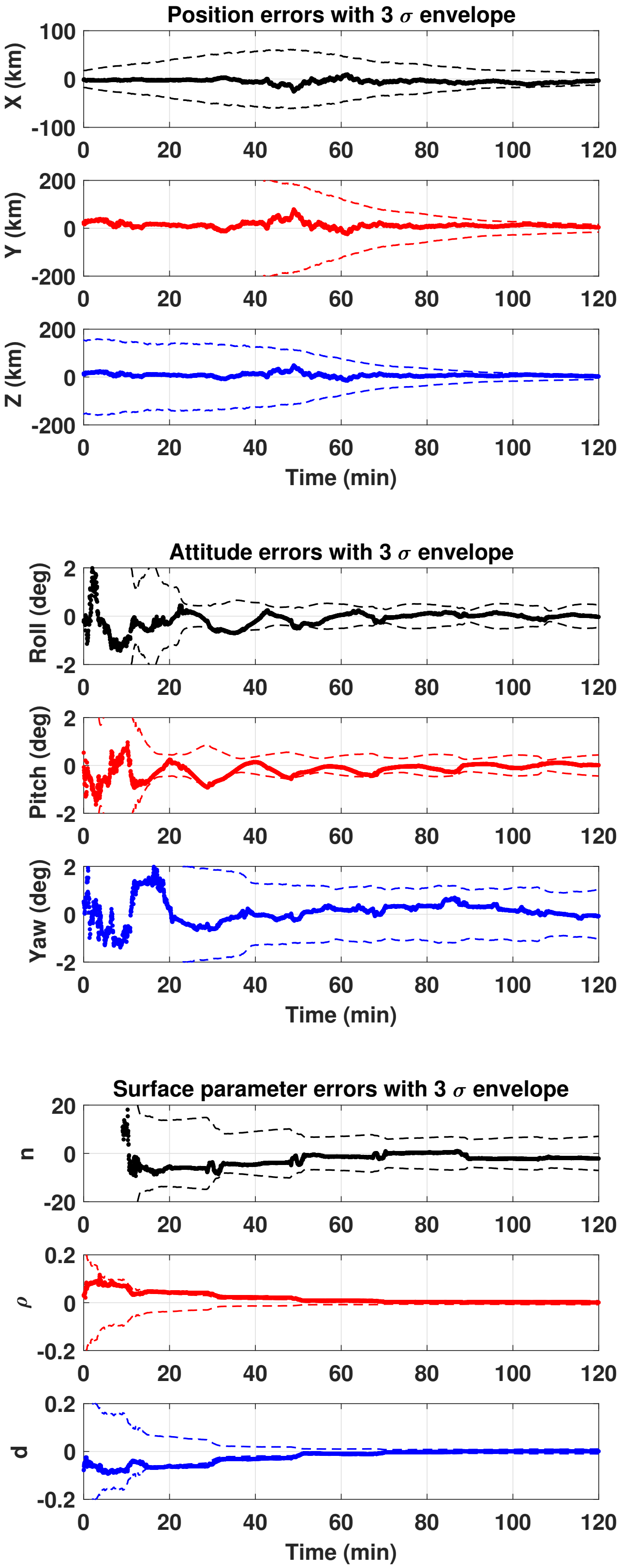

Figure 4: Position, attitude, and surface parameter errors with the PFGMM with the constraint information

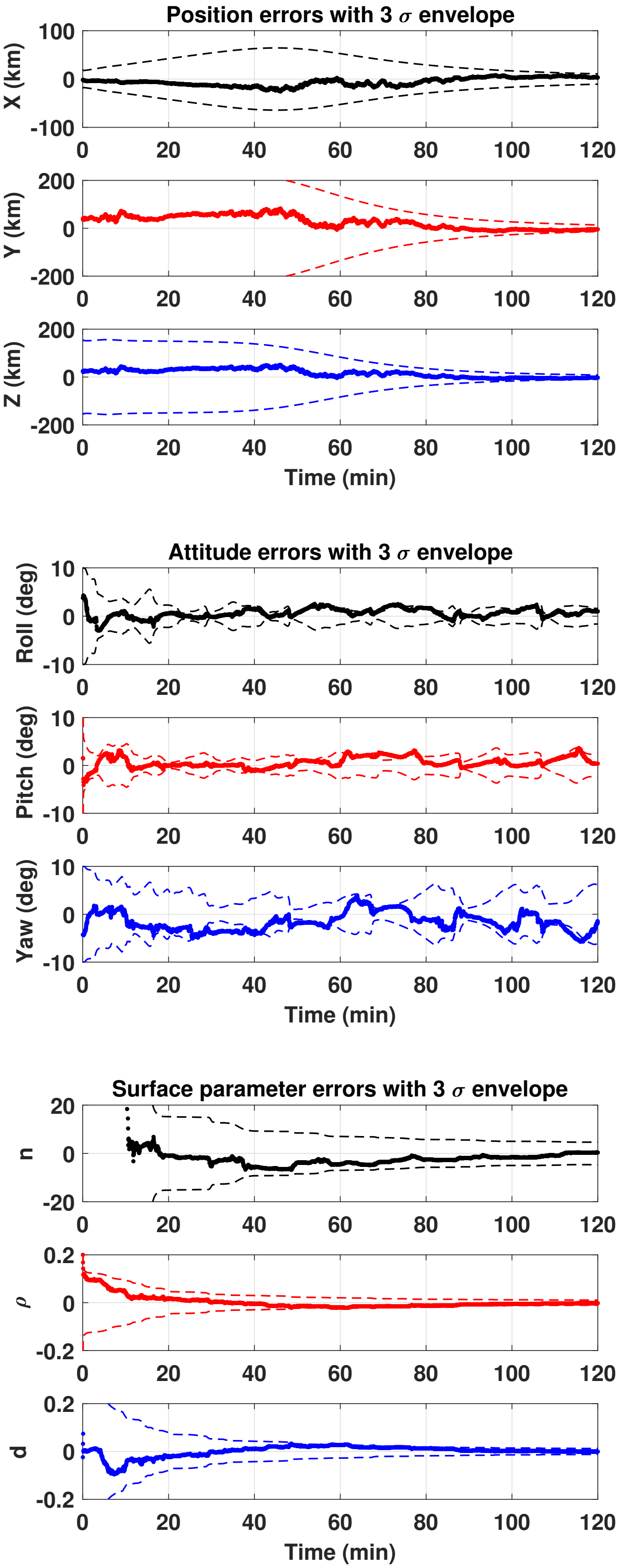

Figure 5: Position, attitude, and surface parameter errors with the TIUKF

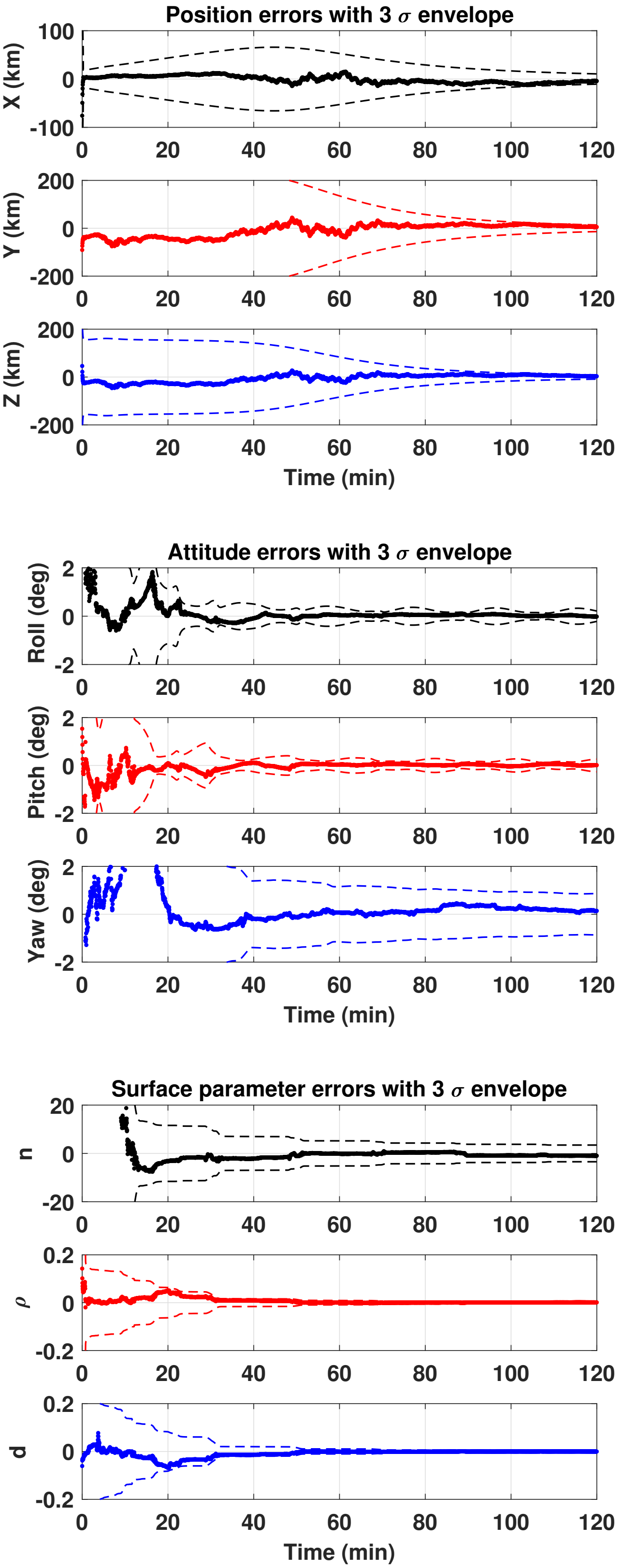

Figure 6: Position, attitude, and surface parameter errors with the TEKF with underweighting

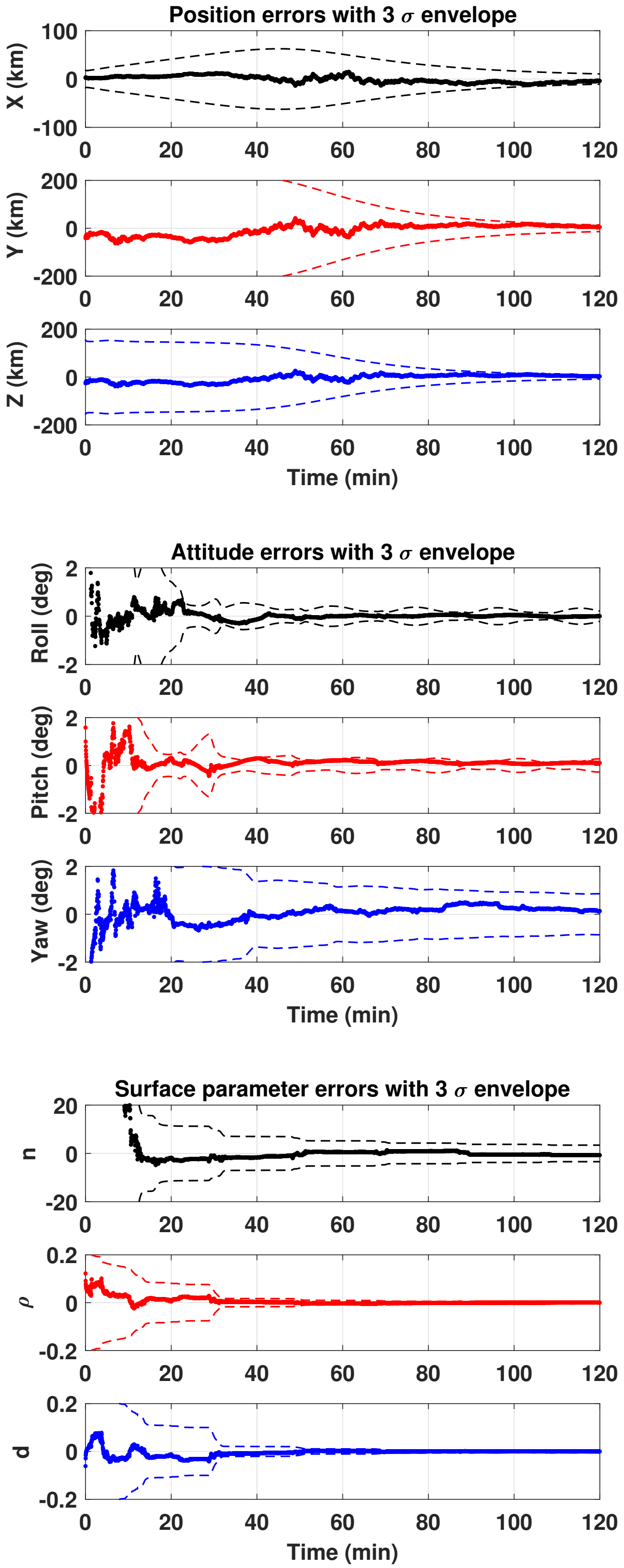

Figure 7: Position, attitude, and surface parameter errors with the TEKF with considering surface parameters

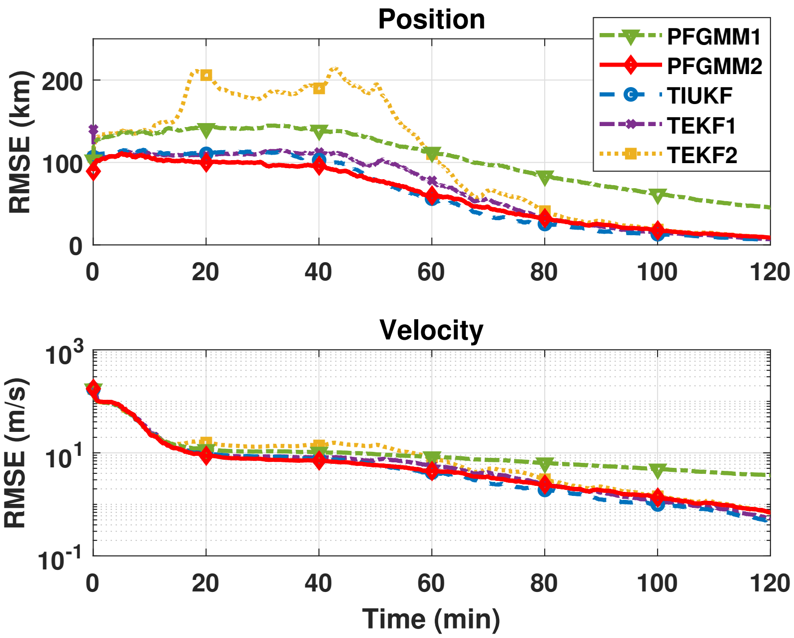

Figure 8: Monte Carlo averaged RMSE of position and velocity for 100 random realizations

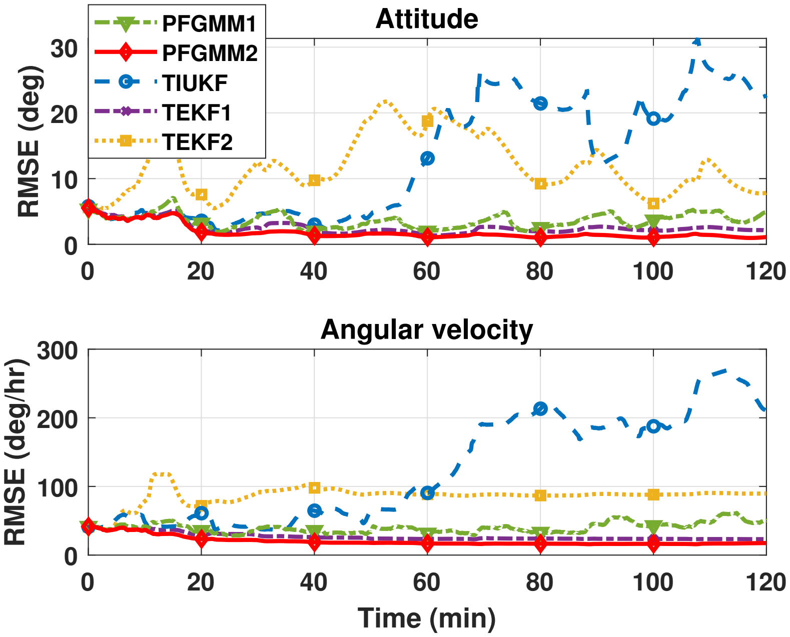

Figure 9: Monte Carlo averaged RMSE of attitude and angular velocity for 100 random realizations

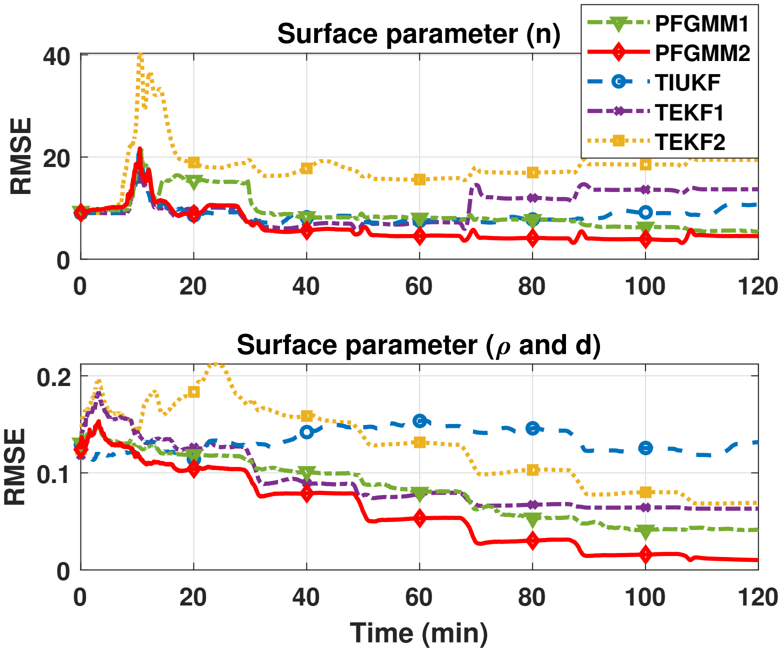

Figure 10: Monte Carlo averaged RMSE of surface parameters for 100 random realizations

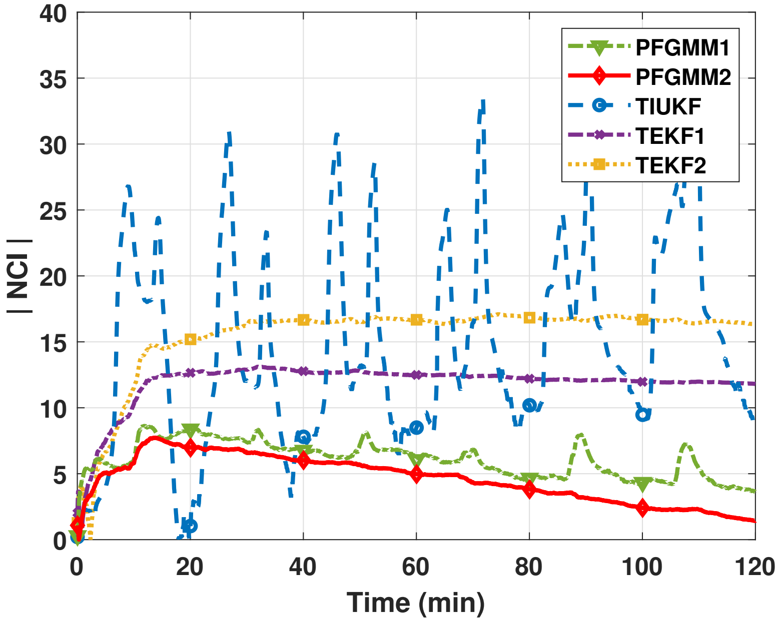

Figure 11: Time history of the absolute NCI value for 100 random realization